Front. Chem. Sci. Eng. 2021, 15(1): 164–179
https://doi.org/10.1007/s11705-020-1976-z

RESEARCH ARTICLE

Charge-carrier photogeneration and extraction dynamics of polymer solar cells probed by a transient photocurrent nearby the regime of the space charge-limited current

Boa Jin[1], Hyunmin Park[1], Yang Liu[2], Leijing Liu[2], Jongdeok An[1], Wenjing Tian[2], Chan Im (✉)[1]

1 Department of Chemistry, Konkuk University, Seoul 05029, Republic of Korea
2 State Key Laboratory of Supramolecular Structure and Materials, College of Chemistry, Jilin University, Changchun 130012, China

© Higher Education Press 2021

Abstract To understand the complex behaviors of photogenerated charge carriers within polymer-based bulk-heterojunction-type solar cells, the charge-carrier photogeneration and extraction dynamics are simultaneously estimated using a transient photocurrent technique under various external-bias voltages, and a wide range of excitation intensities are analyzed. For this purpose, conventional devices with 80 nm thick active layers consisting of a blend of representative P3HT and PTB7 electron-donating polymers and proper electron-accepting fullerene derivatives were used. After the correction for the saturation behavior at a high excitation-intensity range nearby the regime of the space charge-limited current, the incident-photon-density-dependent maximum photocurrent densities at the initial peaks are discussed as the proportional measures of the charge-carrier-photogeneration facility. By comparing the total number of the extracted charge carriers to the total number of the incident photons and the number of the initially photogenerated charge carriers, the external quantum efficiencies as well as the extraction quantum efficiencies of the charge-carrier collection during a laser-pulse-induced transient photocurrent process were obtained. Subsequently, the charge-carrier concentration-dependent mobility values were obtained, and they are discussed in consideration of the additional influences of the charge-carrier losses from the device during the charge-carrier extraction that also affects the photocurrent-trace shape.

Keywords charge-carrier photogeneration, transient photocurrent, polymer solar cells, charge-carrier extraction, space charge-limited current

Received January 2, 2020; accepted June 7, 2020

E-mail: chanim@konkuk.ac.kr

1 Introduction

A number of potential applications where π-conjugated polymers can play important roles exist along with the possibility that flexible and printable solar cells are the most feasible applications among them [1]. Indeed, the power conversion efficiencies (PCEs) of such polymeric solar cells now exceed about 17% [2,3]; however, this is still lower than the PCEs of either novel perovskite-based solar cells [4] or the market-dominant silicon-based solar cells [5]. Therefore, the requisite improvement of the current PCEs of polymer-based organic solar cells needs to be based on a deep quantitative knowledge about the underlying optoelectronic mechanism of the complex device condition.

It is widely accepted that the total PCE (η_{total}) of a solar cell can be expressed as the product of all of the efficiencies for the processes that occur during the solar cell operation, as given by the following equation, $\eta_{total} = \eta_{abs} \times \eta_{CC} \times \eta_{ext}$, where η_{abs}, η_{CC} and η_{ext} represent photon-absorption efficiency, charge carrier (CC)-formation efficiency and CC-extraction efficiency. This classification and terminology can vary by group according to the emphasis of the model-suggestion points [6,7]. Nevertheless, it is relatively clear that it is important, at least at the initial exciton-formation stage before the severe exciton diffusion, to gain an understanding of the number of excitons that can be formed in the active layer of a solar cell together with accurate spectral and spatial distributions. To achieve this, a transfer-matrix method with accurate optical constants was used to analyse the thickness-dependent PCE of polymeric bulk heterojunction (BHJ)-type solar cells consisting of poly[4,8-bis[(2-ethylhexyl)oxy]benzo-[1,2-b:4,5-b]dithiophene-2,6-diyl] [3-fluoro-2-[(2-ethylhexyl)-carbonyl]thieno[3,4-b]-thiophenediyl] (PTB7) blended with [6,6]-phenyl-C71-butyric

acid methyl ester (PC71BM) [8] and regio-regular poly(3-hexylthiophene) (P3HT), blended with, for example, phenyl-C61-butyric acid methyl ester (PCBM) [9]. Since it has become possible to compare an accurate estimation of the internal absorption (i.e., exciton-formation ratio) with the total number of incident photons [8], the spectrally resolved external quantum efficiency (EQE) as well as the internal quantum efficiency (IQE) of the CC photogeneration and extraction for various active-layer thicknesses have been obtained for the PTB7:PC71BM system. It is crucial to notice that the importance of the EQE and the IQE is not only regarding the CC photogeneration, but also the extraction, since even the short-circuit current should also be detected by an external electric detector. For both of the representative polymer systems, similar EQE and IQE estimations of ~60% and ~80% were made at 520 nm, respectively; as a result, ~20% of all of the formed excitons cannot be either sufficiently converted to CCs or extracted to an external device to be detected. It might be noteworthy that the non-fullerene acceptors (NFAs) dominate to achieve higher PCE recently, however fullerene acceptors can play important roles not only to understand insights of polymer solar cells and but also to achieve higher PCE, for example, in conjunction with NFAs [2].

To unveil the CC-formation efficiency from primary excitons, transient absorption spectroscopy (TAS) is often used to visualize the population dynamics of latent charge-transfer states. Since most TAS studies are performed optically with the use of transparent thin films that do not comprise any electrodes, they can provide impressive insights into the formation and decay of the charge-transfer state, but they are often limited in terms of the attainment of more realistic CC dynamics like those of a device. Nevertheless, it is strongly believed that the charge-transfer states that appear in TAS are a precursor for mobile-free CCs, like those of a practical device situation, as shown with the acceptor-blending ratio-dependent charge-transfer-state-forming facility of the PTB7 system, and this is due to a close correlation with the corresponding device PCE values [10]. A previous study shows that the internal loss of ~18% was caused by a direct relaxation of the primary excitons that competes with the charge-transfer-state formation, and this excitonic loss seems to be an inadvertent intrinsic property of the PTB7 system, even with the optimized acceptor blending ratio. Although the exciton-loss ratio that was obtained from the TAS study seems consistent with an IQE loss of ~20% in terms of its estimation regarding devices under the steady state (ss) operating condition, TAS can provide further details under an electric field, as has been shown by a photo-induced absorption study with dye-sensitized solar cells [11].

In particular, to deepen the current understanding of the dynamics of the photo-induced CC formation and the CC extraction from the active layer of a device to an external circuit, the transient photocurrent (TPC) [12] method was chosen. A practical reason for this choice is the inability to obtain reasonable signals for PTB7 with the use of the charge extraction by the linearly increasing voltage (CELIV) method, where the delay times are comparable at the microsecond time scale, whereas a previous study has shown that this is possible for the P3HT system [13]. The difficulty of the use of the CELIV method with the PTB7 system is due to the faster dynamics of the CCs in the PTB7 solar cells, as shown by the previous intensity-dependent TPC results of both the PTB7 and P3HT systems [14].

It is enormously complicated, however, to understand those material-specific TPC results due to the multi-layered device structure, and the simultaneous flow of various underlying processes (i.e., CC photogeneration) such as relaxation and extraction. To separately estimate the CC mobility from these complications, the time of flight (TOF) technique is frequently used within such disordered polymeric systems [15]. The important preconditions for the attainment of a reliable CC mobility are the use of a much thicker active-layer thickness of the ~10 μm order, compared with the typical thickness of the ~100 nm order, to achieve the correct transit time, and the use of a moderate excitation intensity to prevent the serious electric field deformation that is caused by the photogenerated CCs themselves [16]. However, the use of the conventionally thin active layers in this study is intentional, and this is in particular to maintain the consistency with the optimized solar cell structure to avoid any severe change of the underlying mechanisms. In addition, a wide excitation-intensity range was used for the probing of the CC-interaction dynamics with respect to the TPC method.

To gain the insights regarding the conventional thin film samples, clarification of these issues according to the following outline will be presented in this study. As the saturation behaviour at the high excitation-intensity values could be effectively corrected to obtain accurate intensity-dependent CC-photogeneration tendency values, the authors integrated the TPC traces to obtain the number of the extracted CCs from the optimized solar cells; then, these values were used to calculate both the EQEs and IQEs of the CC extraction during the TPC process. By completing those analyses, the correlation between the maximum extractable photocurrent and the space charge-limited current, as estimated with the use of the characteristics of the dark current density versus voltage (dark J–V), was confirmed. These results are presented in the subsection "CC photogeneration and extraction efficiencies".

Then, as is discussed in the next subsection "TPC dissipation and mobility", the shapes of the TPC traces was considered. Due to the analysis of the TPC-trace shape, the influence of the resistor-capacitor (RC) time constant that is due to the thin-film thickness must be considered. The transit times for the estimation of the CC mobility were then presented as functions of the excitation intensity after the suggested corrections were implemented for the RC

limits as well as the saturation effect. At the same time, the TPC traces were discussed in terms of how they were affected by the additional CC loss during the extraction process. It should be noted that, for the entirety of the analysis, a statistical method where a direct dealing with the obtained traces occurred was mainly used instead of any technical fittings with the existing analytical models. Because these existing analytical models with various assumptions can limit to enable an intuitive learning of the essential truths regarding the TPC traces.

2 Experimental

The TPC measurements were performed using two representative organic photovoltaic BHJ solar cells. One is made of P3HT (Rieke, Germany) that has been blended with PCBM (1-Material Inc., USA), and the other comprises a PTB7 (1-Material Inc., USA):PC71BM (1-Material Inc., USA) blend. All the materials were used as purchased.

The blended active layers and the thin layers of the Clevios™ P VP AI 4083 brand of poly(3,4-ethylenedioxythiophene):poly-(styrenesulfonate) (PEDOT:PSS; Heraeus, Germany), were spun-cast onto indium tin oxide-covered glass substrates, and then lithium fluoride/aluminium (LiF/Al) counter electrodes were thermally evaporated. The details of the fabrication processes that were used in the present study including the substrate cleaning and the solution preparation are described in previous studies [8,14]. The obtained device structure is as follows: glass (1.1 mm)/indium tin oxide (180 nm)/PEDOT:PSS (50 nm)/BHJ active layer (80 nm)/LiF (0.3 nm)/Al (120 nm). For the attainment of higher device-efficiency values, the acceptor blending ratios of the P3HT:PCBM and PTB7:PC71BM active layers are 41 and 60 wt-%, respectively.

All the devices were characterized to obtain their device parameters (i.e., open-circuit voltage (V_{OC}), short-circuit current density (J_{SC}), fill factor and PCE) using the J–V measurements under the standard illumination conditions as well as dark conditions. A detailed description of the standard 1-sun test condition, often referred to as the air mass 1.5 G spectral irradiance, at the power of 1 $kW \cdot m^{-2}$ is described elsewhere [8]. Regarding the obtained PTB7 device, the PCE is 8.4%, the V_{OC} is 0.75 V, the J_{SC} is 17.7 $mA \cdot cm^{-2}$, and the fill factor is 63.4%, while the values of the P3HT device are the PCE of 4.6%, the V_{OC} of 0.65 V, the J_{SC} of 11.0 $mA \cdot cm^{-2}$, and the fill factor of 65.5%. Those devices were further characterized by incident photon to current efficiency (IPCE) to obtain IQE as describe previously [8].

To generate the CCs within the active layers for the TPC, the Surelite II-10 neodymium-doped yttrium Al garnet laser (Continuum, USA) was used, followed by the use of an optical parametric oscillator (Continuum, USA). The pulse width of this pulsed laser system is approximately 5 ns at a 10 Hz repetition rate. The dimensions of the rectangular beam size that illuminated the active pixel of 3 mm × 3 mm are 2 mm × 2 mm, and a shadow mask was employed to prevent the possible edge effects. The excitation wavelength is 520 nm (2.38 eV), and the typical excitation-pulse energies are listed in Table S1 (cf. Electronic Supplementary Materials, ESM) part with the corresponding transmittance values of the used neutral density (T_{ND}) filters.

It is remarkable that the 5-ns-long pulse energy of 0.416 μJ means an incident photon density of 2.72×10^{13} photons $\cdot cm^{-2}$, as this is comparable with 2.1×10^4 suns under the assumption that the wavelength of all photons is 520 nm. Although this assumption is extreme, it is helpful if the difference between the pulsed and CW conditions is briefly shown, especially when photons are absorbed to form excitons in the active layers.

The 33521A arbitrary function generator (Agilent, USA) was used to apply external biases. The single delay time between the "bias on" and "laser on" moments is 30 μs, while that between the "laser on" and "bias off" moments is 40 μs. For the tracing of the observed TPC, the TDS 3054B oscilloscope (Tektronix, USA) was used over a 50 Ω load. The data-sampling interval during the whole TPC process is 10 ns. The laser system, the function generator, and the oscilloscope were synchronized using a common electric-trigger signal. The TPC setup including the device structure is schematically presented in Fig. S1 (cf. ESM). And in Fig. S2 (cf. ESM), the full range of a typical TPC record with its integrated trace is also presented.

3 Results and discussion

In Fig. 1, two sets of the smoothed TPC traces at the 0 V bias are shown. The PTB7 time scale in Fig. 1(a) is 0–10 μs, while that of P3HT in Fig. 1(b) is 0–20 μs because of the slower TPC decay of P3HT. These traces are presented with other traces of various external biases in a previous study [14]. The primitive findings from the direct observations of the TPC traces are subsequently described. First, the transients could be clearly separated into the following three regimes, as marked in Figs. 1(a) and 1(b) with arrows: I) initial plateau part, especially above the high incident photon density of ~2.72×10^{13} photon $\cdot cm^{-2}$; II) subsequent rapid-decay part; III) final slow long-tail part. Second, all of those decays show a well-defined exponential functionality. Third, with the increasing of the incident photon density, the initial peaks were increased, and the traces were extended. Fourth, both the initial peaks and the traces were saturated at the higher incident photon densities. Fifth, with the increasing of the external-bias voltages, the peaks were increased, and the traces were contracted. Lastly, as previously mentioned, the dissipation of the PTB7 traces is significantly faster than that of the

P3HT traces, along with pronounced dispersive behaviours [13]. Actually, most of these primitive features are the common characteristics of both systems, and therefore, at a first glance, they can be parameterized as material-specific characteristics with different time scales, as shown in Figs. 1(a) and 1(b).

3.1 Charge carrier photogeneration and extraction efficiencies

To unveil the hidden meanings of the primitive findings, the maximum photocurrent densities of the initial-peak areas were considered as a measure of the CC-photogeneration degree and were plotted, as shown in the inset of Fig. 1(a). This process is plausible because the whole TPC procedure started with the CC photogeneration at the laser-pulse impact moment, and therefore, the initial peaks should directly correlate with the measurement of the detectable CC-photogeneration degree. Interestingly, the plots in the inset of Fig. 1(a) comprise two distinctive parts, as follows: first, quasi-linearly increasing parts at the low incident photon densities, and second, saturated parts at the high incident photon densities. The former parts are slightly sublinear with an exponent of ~0.9 in most cases, and this should be a clear sign that the initial peaks are proportional to the numbers of the photogenerated CCs; the latter parts should indicate the saturation behaviour due to the excessively high incident photon densities, as shown in Table S1. The photocurrent densities at the high incident photon densities are almost constant or converge toward the saturation of the photocurrent densities, depending on the external-bias voltages (i.e., 0.4, 0 and –2 V), and they are virtually independent of the used material systems. It is noteworthy that the transition toward the saturation part did not follow a power law given the typicality of the 0.5 exponents for the excitonic bimolecular recombination (e.g., singlet-singlet annihilation at the high excitation intensities) [16].

The similarly converging photocurrent densities of the two systems at –2 V are closely comparable with their dark current densities at the 2 V forward bias that was obtained from the dark *J*–*V* characteristics in spite of the opposite polarity, as shown in Fig. 2. This implies that the saturation of the TPC density at the high incident photon densities can be explained by means of the space charge-limited current concept, because the dark *J* at 2 V is clearly at the SCLC regime, where the dark current should not be affected by any injection barriers but is mainly limited by its own transport facility. A comparable conclusion was previously reached regarding the space charge-limited

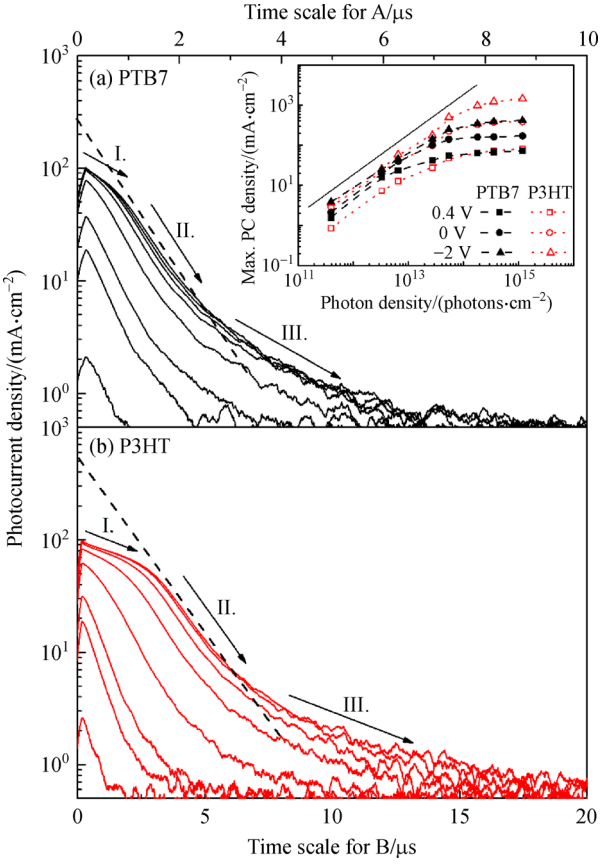

Fig. 1 TPC traces of the following devices at the 0 V external-bias voltage with various excitation intensities: (a) PTB7:PC71BM and (b) P3HT:PCBM (Dash lines are demonstrative extrapolating lines that are based on the tangents of the fast exponential-decay parts of the TPC traces of the cases with the highest incident photon densities. These lines were slightly moved to the upside for an improved readability). Inset in the (a), the post-correction maximum photocurrent density at the initial peak is plotted as a function of the incident photon density. The solid lines with a slope of 1 are shown for the eye-guiding purpose.

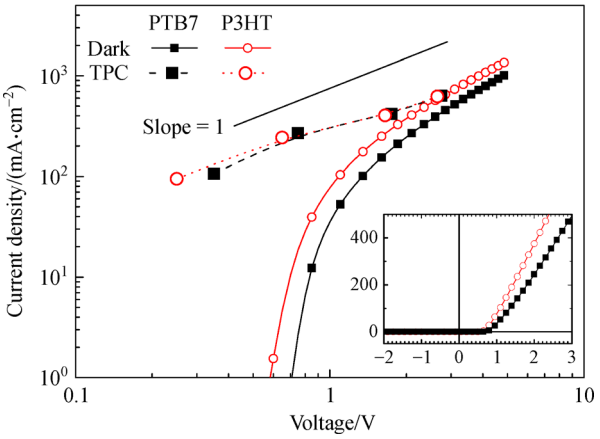

Fig. 2 Dark *J*–*V* plots of PTB7 (solid line with rectangles) and P3HT (solid line with open rectangles), and the maximum photocurrent density at the initial peak vs. voltage (V_{total}) plots of PTB7 (dash line with rectangles) and P3HT (dash line with open rectangles). In the inset, the same dark *J*–*V* plots are shown at a linear scale. An additional solid line with a slope of 1 is shown for the eye-guiding purpose.

current in organic solar cells under the open-circuit condition using an alternating current-admittance method [18].

The space charge-limited current feature is also applicable for the external biases that are less than the injection threshold, although the saturated-PC densities at the 0.4 and 0 V forward biases are many orders of magnitude higher than those of the dark-current densities at the same forward biases. The low current densities at these forward-bias voltages are explained by the fact that they are clearly below the injection threshold in terms of the dark J–V characteristics, while the photocurrent that is caused by the photovoltaic effect must flow in an opposite direction compared with the forward dark current; thus, the photogenerated CCs can be extracted from the active layer without any significant barriers, and this is carried out by its own bulk-transportation property when the photocurrent exceeds the space charge-limited current.

Upon the involvement of the photovoltaic effect, the strength of the electric field that has actually been exercised upon the CCs in the active layer needs to be considered, because the photogenerated CCs must be extracted to the external circuit for their detection under this electric field. Therefore, the internal-bias voltage (V_{int}) that is caused by the intrinsic photovoltaic effect needs to be added to the external-bias voltage (V_{ext}) to form the total-bias voltage (V_{total}) with which the CC extraction can be driven. The V_{int}, however, decreased over time for the pulsed transient method, which is typical, although the V_{total} at the initial-peak area did not necessarily show a dramatic reduction during the μs time scale, as shown by various transient photovoltage studies [19,20]. Thus, the V_{total}, especially at the beginning of the TPC procedure, was calculated using Eq. (1) together with the formal V_{int} that was taken from the V_{OC} of the PCE characterization, as shown in the "Experimental" section.

$$V_{total}(t) = V_{ext} + V_{int}(t). \quad (1)$$

As expected, the plots of the saturated-TPC densities versus the V_{total} seem to follow the space charge-limited current trend of the dark J–V even below the injection-threshold range, as shown in Fig. 2. It is impressive that the simply constructed V_{total} behaves reasonably, although numerous additional aspects need to be considered to obtain an accurate internal electric field distribution [21,22]. The simple V_{total} herein was applied for the CC-mobility estimation that is described later in this study, and its plausibility was confirmed while an intuitive overview was also maintained.

Now it is possible to assume that the plateau that appeared at the beginning of the TPC traces at the high incident photon densities was mainly caused by the saturation, thereby implying that the CCs were generated proportionally to the incident photon density; however, the electrically detected peaks, and therefore the mobile CCs, were limited by the saturation. Given this, a correction method for the saturation effect was suggested to more accurately reveal the CC photogeneration with the obtained TPC data. For this purpose, the second rapid-exponential-decay part was chosen, because at the low incident photon densities, where there is no plateau feature, exponential slopes that are similar to those at the high incident photon densities are consistent. Therefore, a hypothetical suggestion was presented, where the TPC traces with the plateau feature, which also comprise a well-defined monotonic exponential-decay pattern without any plateau, were employed if the corresponding space charge-limited current did not result in the saturation at the high incident photon densities. A further precondition is actually required for this suggestion to ensure accuracy, where the excess CCs that could not be extracted in time due to the space charge-limited current bottleneck remain immobilized and dissipated in the active layer to prevent any shift or change of the mutual-decay pattern. To apply this correction, an extrapolation of the tangents was performed based on the rapid-decay parts of the saturated-TPC traces, as shown in Fig. 1. Further, the corrected PC-density values were taken from the intersections with the extrapolated lines and the vertical axis at the laser-pulse impact moment.

Notably, the slopes of the rapid-exponential-decay parts are very similar to those of the charging curves, regardless of the incident photon densities and the materials, because the TPC responses of the thin samples of an 80 nm thickness must be bound with the fastest charging response of the whole circuit. Therefore, it is necessary to exhibit a similarity between the dominant decay pattern and the charging curves that can be specified by the 0.45 μs RC time constant of the entire TPC setup, including the target devices. Further explanation to estimate the RC time constant was reported in our previous study [14]. The detailed discussion will be continued in the subsection "TPC dissipation and mobility" of this paper, where the shapes of the TPC traces are further analysed.

Interestingly, the linear dependency of the sublinear dependencies of the uncorrected plots could be recovered with a slope of 1 after the previously mentioned correction, as shown in the inset of Fig. 1(a). The need to further verify the validity of the correction is certain, however, because the saturation can change the decay behaviours; for example, the slopes of the rapid-decay parts were flattened with the increasing of the incident photon density,

Table 1 Overview of the bias convention used in this study

V_{ext}/V	V_{total} PTB7/V	V_{total} P3HT/V
0.4	–0.35	–0.25
0	–0.75	–0.65
–2	–2.75	–2.65

especially for the P3HT system, as shown in Fig. 1(b). Nevertheless, the corrected incident photon density dependency shows an impressive linear trend that strongly supports the proportionality of the TPC peaks to the photo-induced CC-photogeneration degree. It might be of interest that some of the previous intensity-dependent ss PCE experiments reported similar sublinear dependencies [23], which are closely comparable with the uncorrected results of the previous study [14].

As the next step, all of the TPC traces were integrated to obtain the total number of the extracted CCs after the CC photogeneration, as shown in Fig. S2. The obtained numbers of the extracted CCs are plotted as functions of the incident photon density in Fig. 3(a). The slopes of the P3HT cases are close to ~0.9, while the slopes of the PTB7 cases are close to ~0.7 for the initial increasing regime. Also, it appears that the saturation regime is similar to those of the maximum PC-density plots, as shown in the inset of Fig. 1. Actually, the slopes of the linearly increasing regime of the P3HT are independent of the V_{ext}, while the PC-density magnitude and the saturation level clearly increased with the increasing of the V_{ext}. The trend of the PTB7 system is also similar to that of the P3HT system, but the slopes of the former at the linearly increasing regime are significantly smaller than those of the P3HT, and subsequently, the saturation levels at the same V_{ext} also decreased.

To discuss the results systematically, the EQE and the IQE of the photogenerated-CC extraction were calculated and are plotted in Figs. 3(b) and 3(c) according to the following Eqs. (2) and (3), respectively:

$$\mathrm{EQE}(\%) = \frac{\text{number of total extracted CCs} \times 100}{\text{number of total incident photons}}, \quad (2)$$

$$\mathrm{IQE}(\%) = \frac{\text{number of total extracted CCs} \times 100}{\text{number of total absorbed photons}}. \quad (3)$$

The conventional EQE, often referred to as the IPCE, as well as the IQE were typically estimated using an ss method, while the estimation condition of this study is a pulsed transient condition. The equations were only slightly modified by the changing of the terminology regarding the CCs from “photogenerated” to “extracted”, as this emphasizes that the CCs, namely a short laser-pulse excitation-induced current, should be detected over an external resistance of 50 Ω using an oscilloscope.

The intensity-dependent EQE plots in Fig. 3(b) show the following two distinctive regions: a region that is moderately intensity-dependent at the low incident photon densities, and a steeper decreasing region at the high incident photon densities that is similar to that of the extracted CCs. The latter steeper decreasing parts with the slope of about −1 should be related to the saturation

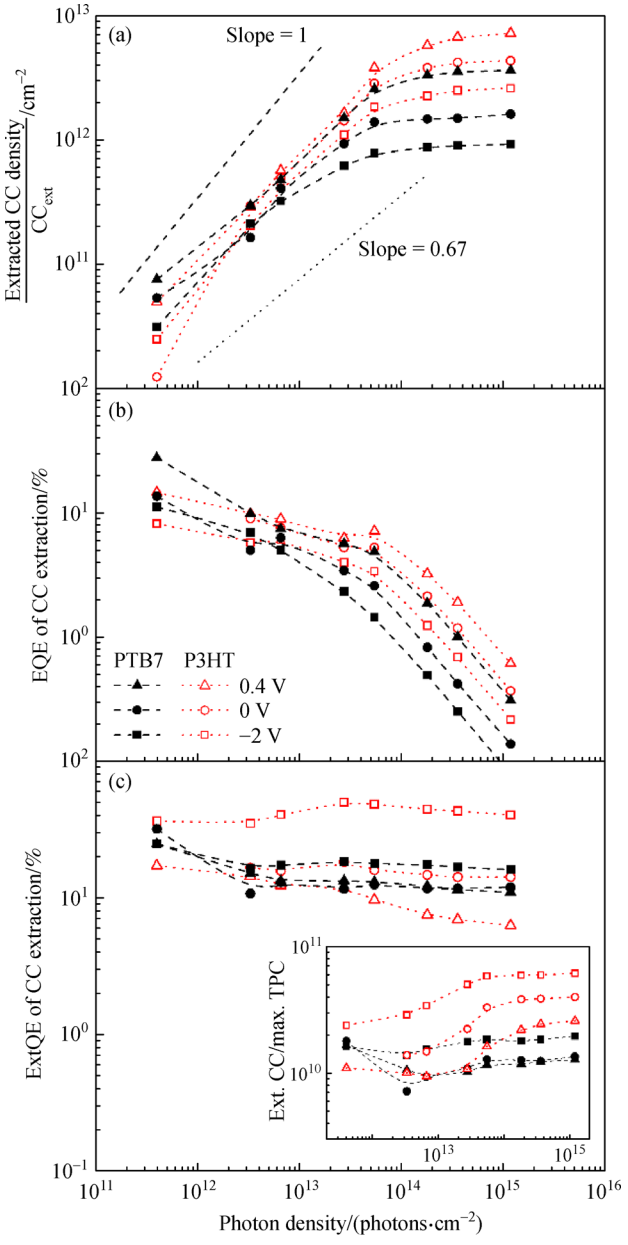

Fig. 3 (a) Numbers of the extracted CCs, as calculated from the integration of the TPC traces; (b) the EQE; (c) the ExtQE, as functions of the incident photon density. The solid lines with slopes of 1 and 0.67 are shown for the eye-guiding purpose.

features at the high incident photon densities, and except for the parallel shifting of the curves, this trend is material-independent. The EQE slopes of the P3HT at the low incident photon densities, however, are significantly flatter than those of PTB7, thereby implying that PTB7 might comprise additional and/or faster loss channels, which depends on an intensity that is stronger than that of P3HT.

The EQEs under the conventional ss condition at the 520 nm excitation wavelength are approximately 60% for

both of the material systems [8,25], while most of the TPC EQEs are less than ~10%. In consideration of the performance of the TPC experiment for which a laser-pulse excitation that is at least three orders of magnitude higher than the incident photon density was used during the pulse duration, this is not a surprising difference. Obviously, the TPC EQEs of ~30% for P3HT and ~40% for PTB7 can be obtained with the use of an extrapolation of the flat parts toward the incident photon density of $\sim 1 \times 10^9$ photons$\cdot$cm^{-2}, which becomes comparable with the 1-sun situation.

The TPC IQE can be obtained according to the schema in Fig. 4, if it can be assumed that a reduction of the absorption efficiency, which, for example, is due to a ground-state photobleaching at a high intensity, has not occurred. The experimental ss EQE and IQE of PTB7 at 520 nm are ~60% and ~80%, respectively [8], thereby implying that ~25% of the total incident photons cannot be converted into excitons in the active layer due to reflections at the interfaces, as an example. Further, the main cause of the 15% loss of the EQE (i.e., 20% loss of the IQE) is the competitive monomolecular recombination of the primary excitons for the formation of charge-transfer states [10]. Actually, a remarkable bimolecular recombination did not occur during the QE loss when an optimized device was used for the ss characterization.

The situation was changed, however, upon the use of a short intense-pulse excitation, as shown in Fig. 3(b). The TPC EQE decreased to ~10% from the ss EQE of ~60%, even at the low incident photon densities, and this substantiated the dramatic increase of the CC loss under the short-pulse condition. Under the assumption of the same exciton-forming process (i.e., the same photon absorption), and with the efficiency of ~75%, as estimated under the ss condition in a previous study [8], the TPC IQE of ~13% can be calculated. Ultimately, if a ~30% exciton loss occurs due to the application of a pronounced exciton-exciton annihilation loss under a high-intensity condition [10], the CC loss of ~70% occurs under the pulse situation. Further, under the pulse condition, ~13% of all of the excitons could survive and be extracted as CCs to the external detector after the conversion of the excitons into CCs.

It is important to verify whether the initial peaks are actually a measure of the photo-generated CCs and the nature of their relation to the residual-TPC trace to depict the CC-extraction process. For a further analysis, the dimensionless ratios (E/G ratio) according to Eq. (4) were calculated to testify the functional dependence of the extracted-CC number on the uncorrected maximum TPC densities at the initial-peak area as a measure of the CC-photogeneration degree, and the result is presented in the inset of Fig. 3(c). Surprisingly, the PTB7 plots show flat dependencies, while the P3HT plots show slightly increasing functionalities with an increasing intensity; this is a sign that the generated but immobilized CCs of P3HT that are due to the space charge-limited current saturation can be extracted after a delay, while this is not possible for PTB7, and the latter shows virtually constant relations between the numbers of the extracted CCs and the amplitudes of the TPC peaks as functions of the incident photon density. With this encouraging result, a further effort was exercised to obtain a practical number for the CC-ExtQE according to Eq. (5), as follows:

$$\text{E/G ratio} = \frac{\text{number of total extracted CCs}}{\text{maximum TPC@initial peak area}}, \quad (4)$$

$$\text{ExtQE}(\%) = \frac{\text{number of total extracted CCs} \times 100}{\text{number of total photogenerated CCs}}. \quad (5)$$

For the ExtQE, the maximum TPC densities at the initial-peak areas, which are shown in the inset of Fig. 1(a),

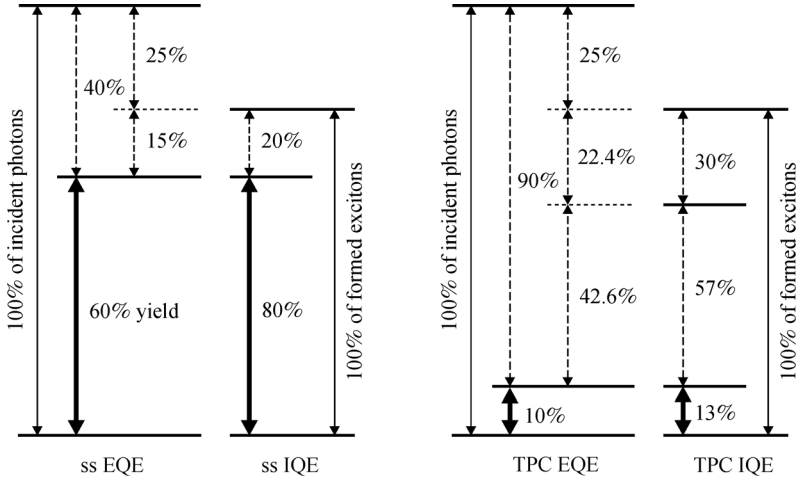

Fig. 4 Schema to compare the EQEs and the IQEs under the ss and TPC conditions of the PTB7 case.

were taken as the measures of the spontaneously photogenerated CCs after the saturation-effect correction, and their plots are shown in Fig. 3(c). The maximum PC-density values were converted to the number of the photogenerated CCs using a conversion factor of 2×10^{10} ($CCs/mA \cdot cm^{-2}$) that was derived from the depicted relation in Fig. 4. The resultant incident photon density-dependent ExtQE plots in Fig. 3(c) show the impressive change compared with the EQE version, especially for the high incident photon densities. It should be noted that the first values at the lowest incident photon density seem unstable because of the worse signal-to-noise ratio at the very weak intensities. The correction for the saturation seems effective, since the negative EQE slopes in Fig. 3(b) are not more significant for the ExtQE, although the P3HT shows some residual reduction trends at the high incident photon densities. Interestingly, P3HT shows a strong electric field dependency, whereas PTB7 shows a weak electric field dependency. The TPC traces of P3HT at 0.4 V show mostly high ExtQEs with a value of ~30%, while the other cases show values that are slightly higher than ~10%. Actually, this ExtQE is an extraction probability of the photogenerated CCs that survived during their transport through the BHJ active layer and passing through the interfaces.

3.2 TPC dissipation and mobility

This study shows that the peak photocurrent densities can be treated as reliable measures of the numbers of the photogenerated CCs, and therefore, they can be used to calculate the ExtQE in combination with the numbers of the extracted CCs. In addition, the TPC traces can provide further information about the CC-extraction dynamics with the timely evolution of the CC amounts that passed through the external resistance where the time-resolved voltage drops were detected. It is often complex, however, to understand those transients because of the inadvertent terms that are related to the reduction of the mobile CCs during the TPC process, both by the arrival of the CCs at the external circuit and by the other effects that can cause the reduction of the CCs before their arrival. The *in-situ* CC losses can shorten the unperturbed transit time that originates from the ordinary dissipation of the TPC traces owing to the arrival of the CCs. It is noteworthy that the transit time can be seriously affected by a dispersive transportation of the CCs in a disordered system that is typical for polymeric materials [15]; therefore, in this study, "dissipation time" is used instead of "transit time" with respect to the fade out time of TPC traces.

The possible reasons for the additional losses are the temporal immobilization of the CCs that is due to the CC trapping [25,26], and the irreversible annihilating reduction of the CCs that is, for example, due to the monomolecular as well as the bimolecular electron-hole (e-h) recombination [27]. At the same time, the amplitude as well as the shape can be affected by the interfaces between the various layers in devices, and these can exhibit parasitic series and/or shunt resistances in addition to inadvertent resistances that are bound in the circuit. It is known that the series resistance of a circuit can majorly affect the TPC-trace shapes [28]; this is often discussed in the form of the RC time constant [29], and it becomes more meaningful for thin-layer devices because of their faster TPC response times compared with the larger RC time constants [30]. Recently, a study was reported to show a sophisticate analysing method of TPC decay kinetics by combining the electrochemical impedance spectroscopy with the TPC method [31].

For a systematic comparison of the traces, they were normalized with the initial-peak values, as shown in Figs. 5(a), 5(b) and 5(c) for PTB7 and 5(d), 5(e) and 5(f) for P3HT for various V_{ext} values. From the normalized traces of both material systems, the inflection points between the first- and second-, as well as the second- and third-, decay parts could be more clearly recognizable than the pristine traces of Fig. 1. Interestingly, the slopes of the two systems are clearly distinguishable, although the TPC patterns can be similarly separated into three phases regardless of the materials. As shown in Table 2, the P3HT decay-time constants are ~4-fold slower than those of PTB7.

Correspondingly, the durations of the P3HT initial-plateau parts are longer than those of PTB7, with the factors of ~3.5, ~3.4 and ~2.7 at $0.4V_{ext}$, $0V_{ext}$ and $-2V_{ext}$, respectively. Undoubtedly, the rapid decay at the initial-plateau range is correlated with the faster dissipation of all the TPC traces, thereby implying that the PTB7 CC mobility is higher than that of P3HT; however, the P3HT decay time is additionally extended due to the longer survival of the CCs that are maintained by the space charge-limited current effect, which is discussed later in this section. The dissipation time constants slightly decreased with the increasing of the V_{ext}, but the bias dependencies of the dissipation time constants are marginal, while the ratios between the PTB7 and P3HT time constants increased significantly with the increasing of the bias voltage. This feature might be explained by the different limiting effects of the RC time constant regarding the systems, which is also discussed in detail later in this section. Interestingly, the first-decay time constants are very similar to those of the third-decay parts, although the magnitude of the photocurrent of the third-decay regime is far less than 10% of the initial photocurrent level.

The 1/e times ($\tau_{1/e}$) until the TPC traces were reduced to 1/e (i.e., 36.8% of the maximum PCs at the initial-peak areas) were chosen as the CC-dissipation time, which includes not only the CC arrivals but also the terms of CC losses. Actually, this $\tau_{1/e}$ is advantageous not only for a direct comparison with the RC time constant, but also for a very simple in-practice attainment. Therefore, the $\tau_{1/e}$ values were taken from the traces in Fig. 5, although the

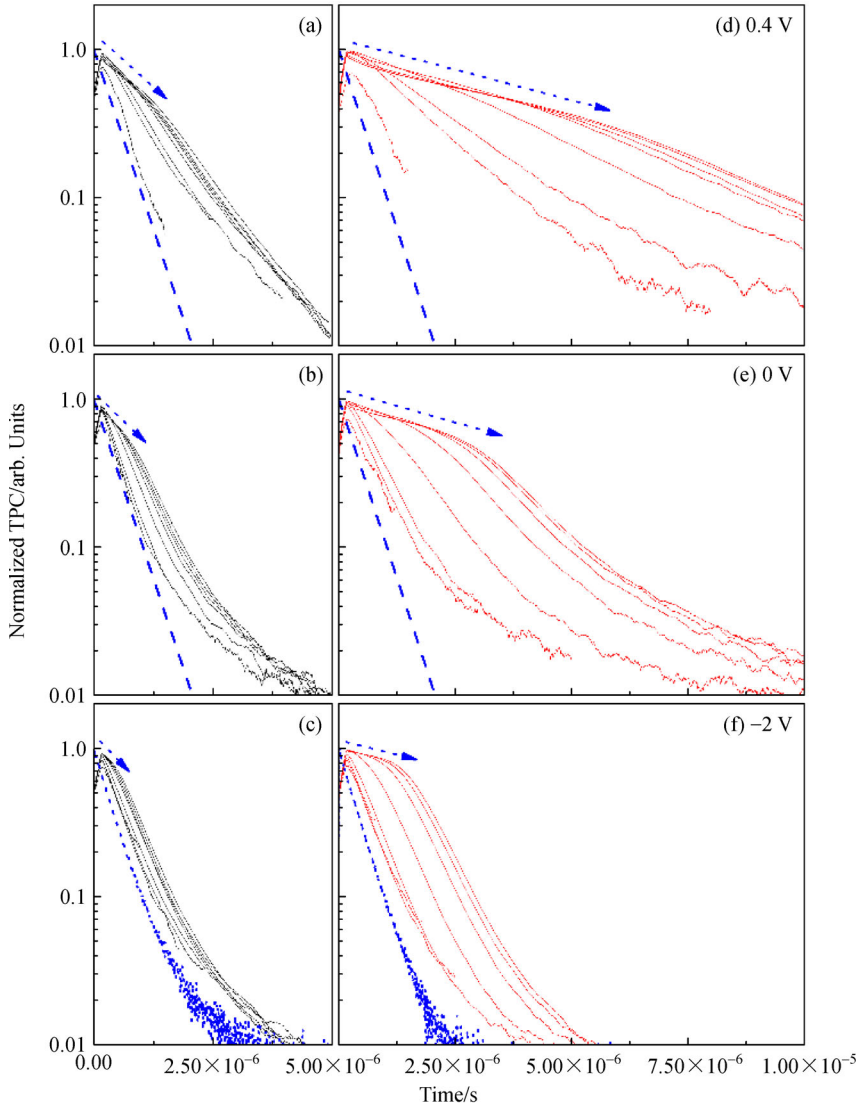

Fig. 5 Normalized TPC traces of PTB7 at (a) 0.4 V, (b) 0 V, and (c) –2 V, and those of P3HT at (d) 0.4 V, (e) 0 V, and (f) –2 V. The dash-dot lines in (a), (b), (d) and (e) are the calculated RC decays with the 0.45 μs time constant, while the dot lines in (c) and (f) are the experimentally estimated dark charging curves. The dot lines at the initial parts are the eye-guiding lines for the slopes of the first parts of the TPC traces.

Table 2 Average time constants (τ) of the first-decay parts

Item	τ at $0.4V_{ext}$	τ at $0V_{ext}$	τ at $-2V_{ext}$
PTB7	1.83 μs	1.45 μs	1.34 μs
P3HT	6.18 μs	5.72 μs	6.08 μs
P3HT/PTB7	3.4	3.9	4.5

traces that are shown therein did not follow a strict mono-exponential behaviour, especially at the high incident photon densities.

One further intentional reason underpinned the choice of $\tau_{1/e}$ is the exclusion of the third-decay parts, because the electric fields at these third parts should be considerably different from those at the beginning, thereby meaning that the underlying mechanism should be very different. Actually, a photovoltaic internal electric field should be formed in a device upon a laser-pulse illumination, and this should disappear as the number of the CCs inside the active layer is decreased over time.

The $\tau_{1/e}$ plots versus the incident photon density shown in Fig. 6(a) are electric field dependent and bimodal. Interestingly, the $\tau_{1/e}$ times converge to a common value with the decreasing of the incident photon density, and this value became closer to the RC time constant of 0.45 μs. As an alternative to the $\tau_{1/e}$, the other times ($\tau_{1/e.2nd}$) that are based on the second-exponential-decay parts can be used, as shown in Fig. 6(b). The saturation effect on the $\tau_{1/e.2nd}$ times should be less, and therefore the $\tau_{1/e.2nd}$ times seem closer to the RC time constant of 0.45 μs than the $\tau_{1/e}$ times. It seems that the mobility of PTB7 is higher than that

of P3HT at the same bias voltage and incident photon density due to the shorter $\tau_{1/e}$ and $\tau_{1/e.2nd}$ times, but this is only under the assumption of the absence of significant additional CC losses. Interestingly, the saturation effect corrected the $\tau_{1/e.2nd}$ times of P3HT at the high V_{ext} and incident photon density values that were overlapped with those of PTB7, thereby showing the material-independent limit caused by the RC time.

Notably, the trends of the $\tau_{1/e.2nd}$ versus the incident photon density in Fig. 6(b) are amazingly analogue to the functional dependences of the E/G ratio (Ext. CC/max. TPC) versus the incident photon density, which are shown in the inset of Fig. 3(c). The intensity-dependent increasing functionality of P3HT is one of the most impressive similarities, and it implies that the reserved-CC extraction of P3HT is longer, which contributed to the increasing of the ExtQE as well. Those findings should be considered as strong evidence of the close correlation of the TPC-trace dissipation times with the CC-extraction efficiencies from the total photogenerated CCs. From the observations, a multistep process during a TPC session could be proposed, where a very fast CC-photogeneration step, including the exciton formation and dissociation, is followed by a relatively slow CC-extraction step, where the formed CCs move toward an external detector without severe losses during the decay of the TPC traces under the space charge-limited current regime. The ExtQE plots in Fig. 3(c), however, and particularly at the high incident photon densities, show an additional intensity-dependent reduction of the extraction efficiency that can be assigned as a bimolecular recombination of the movable electrons and holes, even after a quasi-equilibrium condition is reached, and this is owing to a CC concentration that is higher than the space charge-limited current level.

In fact, an additional fast-decay feature was electrically detected at the beginning of the TPC traces at the high incident photon densities, as shown in Fig. 7. Under the

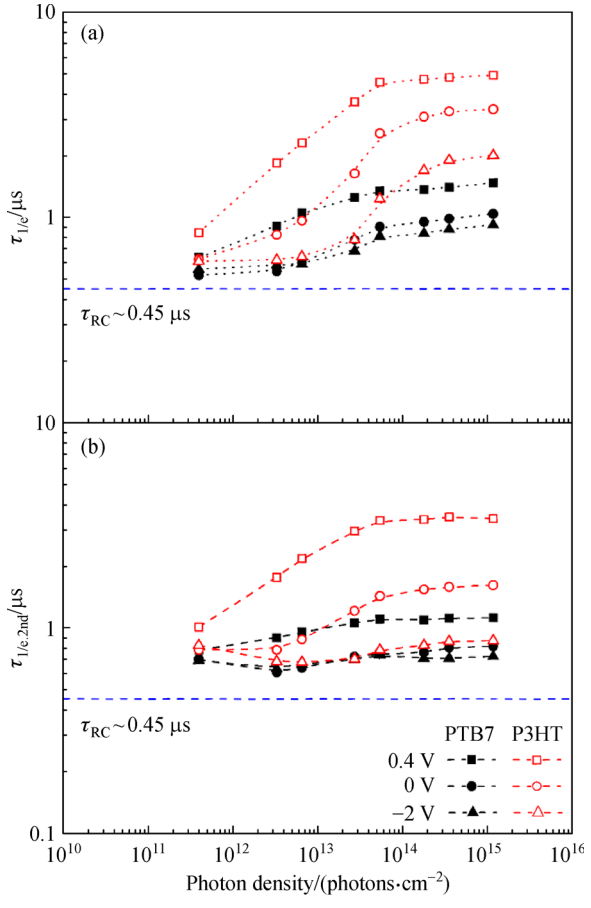

Fig. 6 Plots of (a) $\tau_{1/e}$ vs. the incident photon density and (b) $\tau_{1/e.2nd}$ vs. the incident photon density. The horizontal dash lines mark the RC time constant of the used device of this study.

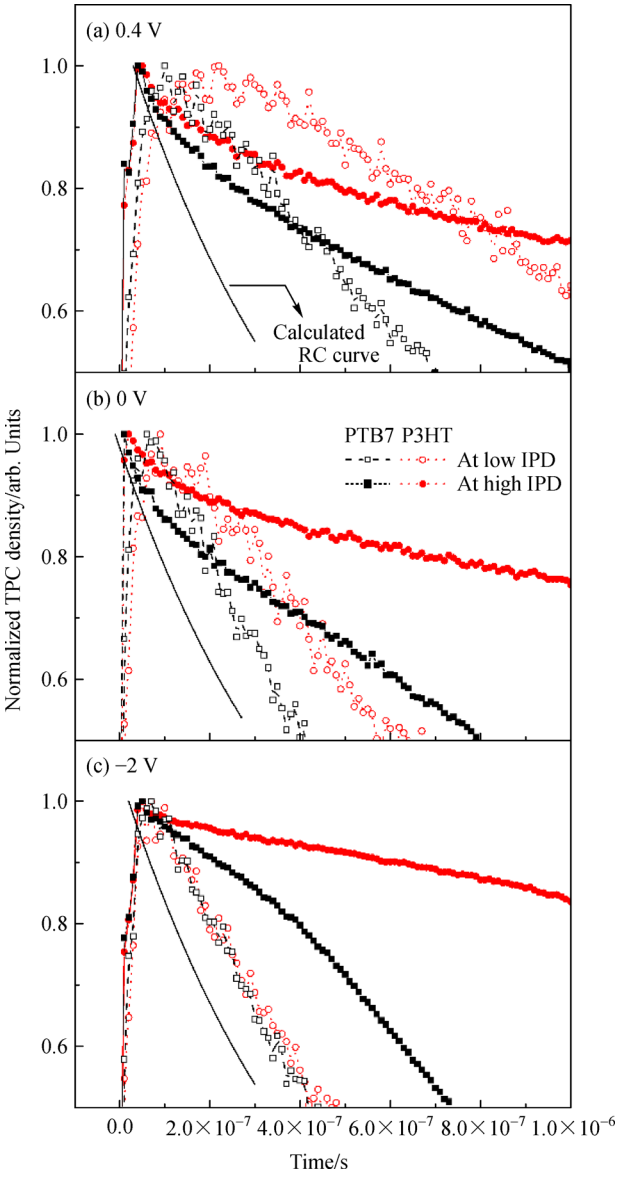

Fig. 7 Magnification of normalized TPC traces at the following external biases at linear scales: (a) 0.4 V; (b) 0 V; (c) –2 V. The dash lines are the calculated RC decay curves.

0.4 V and 0 V external-bias conditions, these features are similar, but at –2 V, this feature is not evident. This finding can be understood with the consideration that the CCs can be instantaneously extracted because of the strong driving force exercised by the electric field with the $-2V_{ext}$. And therefore, the chance of the CCs to dissipate despite the high CC concentration during the pulse impact moment is less. The decay time constants of those rapid-decay parts are close to the RC time constant independent of the material. These fast times, which could be detected by an electric method, are reasonably well correlated with the charge-transfer-state recombination time of ~10 ns [10]; although, this is at least one order of magnitude longer, and this is probably due to the RC delay. Further, their electric field dependent feature strongly supports the finding that this fast decay during the initial-peak area should be the result of the CC-interaction-induced bimolecular recombination [27].

By showing the whole range of the intensity-dependent TPC traces as a three-dimensional map, as shown in Fig. S3 (cf. ESM), a transition point that is located near the incident photon density of $\sim 3 \times 10^{14}$ photons·cm^{-2} starts to appear, and a clearly recognizable shortening of the initial decay occurs at the same time. This CC loss that occurs during the extraction can be expressed as a rectangle-marked transient, as shown in the inset of Fig. S3. The CC-loss function was calculated using the TPC-trace A at the high incident photon densities, and it shows a serious deviation from an exponential functionality, while an exponential functionality is dominant regarding the calculation with the TPC-trace B at the low incident photon densities. This is also the reason why the saturation-effect correction could be performed using the second-decay parts. However, the delayed CC extraction due to the saturation is not directly connected to the CC loss, and this is particularly the case for P3HT. Therefore, the loss function needs to be reduced correspondingly, while the second-decay parts may not be shortened by the CC reduction. The rapid, immediate decaying at the beginning is correlated with the rapid rising of the TPC peaks at the high incident photon densities, while the delayed decaying is correlated with the delayed rising of the TPC traces at the low incident photon densities. The speed of the delayed feature at the low incident photon densities and the weak electric field in Fig. 7(a) increased with the increasing of the electric field strength. Finally, the overlapping of both P3HT and PTB7 nearly occurred at $-2V_{ext}$ because of the strong electric field and the RC-time-constant-limited CC-extraction facility of the whole system. However, the shapes of the peaks at the low incident photon densities and the weak electric field might be explained by the internal CC distribution in addition to the population.

Actually, the TPC method used in this study for the investigation of the CC dynamics is conceptually the same as the TOF method that has been intensively used to investigate the CC-transport phenomena within highly disordered organic random-solid systems [15]. It is also well known that the CC-hopping formalism was developed to clarify the relation between the transport mechanism and the disorder degree, especially according to the interpretation of the TOF results in conjunction with the Monte Carlo simulation method [32]. For the TOF technique, one important precondition is the preparation of a thicker active layer for the attainment of a reliable estimation of the CC-transit time. For the Beer-Lambert calculation, as shown in Fig. S4 (cf. ESM), the optical density of 0.22 was estimated with the use of a ~79 nm thick thin film on a glass substrate. However, a significant interference effect, which can cause a severe deformation of the internal intensity distribution, mainly due to the effective reflection by the metallic electrode as well as the thin active-layer thickness, should be evident. To take into account the interference effect precisely, a transfer matrix method calculation was previously performed with accurate optical constants (i.e., extinction coefficient and refractive index) [8]. An optical field profile of a 79 nm thickness for the 520 nm wavelength was also compiled and it is presented in Fig. S4.

As expected, the 79 nm profile using transfer matrix method shows a clear interference effect compared to the monotonic-decaying profile using the Beer-Lambert calculation. Although the interference effect makes the internal intensity profile shallower than that of the Beer-Lambert calculation, it is still significantly broader than that of the TOF, which is presented with the same optical density but for a 2 μm thickness, as an example. Actually, with a shallower CC layer at the front side of a thick device, as shown in the inset of Fig. S4, it is possible to directly estimate not only a direct observation of the accurate transit times, but also the CC dynamics under the nonequilibrium condition. Despite these advantages, several drawbacks, in addition to the preparation difficulty, hamper thicker devices. For example, many of the applications where disordered polymeric organic solids are used require a typical thickness in the order of ~100 nm, and it is now well known that the morphologies of such organic/polymeric films can be significantly different when the thicknesses, and therefore the preparation conditions, are changed [33,34]. Therefore, the TPC studies for which practical thicknesses are used are meaningful in spite of the specific complications.

Finally, the CC mobilities were calculated with the $\tau_{1/e}$ as transit times and the V_{total} according to Eq. (1) as effective overall electric field strengths that can be exercised on the CCs, and the results are shown in Fig. 8(a). The horizontal lines represent the hypothetical mobilities for which an RC time (i.e., the fastest response times of the given circuit at each V_{ext}) was used. Obviously, the resultant mobility trends versus the incident photon density seem bimodal, and the flat trend at the low incident photon densities can be surely explained by the RC-time

limiting; this finding can be recognized easily by comparing the trends with the hypothetical RC mobilities at the same electric field strength. Similarly, the slower-than-expected trend of PTB7 at $-2V_{ext}$ can be confirmed as the RC-time-limiting effect. To improve the results by correcting the RC-time effect, a well-defined deconvolution of the TPC traces [35] is needed; however, for a practical simplicity, a simple correction was performed through the subtraction of the RC time from the estimated dissipation time.

In Fig. 8(b), the shown CC mobilities were calculated using RC-time-corrected dissipation times; furthermore, the corrected CC mobilities are correspondingly faster along with the recovery of the linear incident photon density dependency, especially at the low incident photon density parts. The trends at $-2V_{ext}$, however, did not seem to be recovered at any linearity, as is explained previously with respect to the excessive dissipation behaviours, and this is due to a highly effective extraction of the CCs. In addition, a further corrective step was made to improve the saturation effect using the dissipation time that was obtained from the second part of the traces, as shown in Fig. 7(c). The idea for the saturation correction is the ability of the TPC traces to follow a similar trend at the high incident photon densities, as if a major space charge-limited current-governed situation is not an issue. This saturation correction seems quite effective, and even CC-mobility trends that are virtually electric field independent were obtained after the saturation-effect correction, as shown in Fig. 8(c).

Actually, the RC-time and saturation-effect corrections mean that the intensity-dependent CC mobilities were determined by the quasi-monoexponentially-extended transit-time feature (i.e., dissipation times), depending on the photogenerated-CC numbers in the active layers. In this study, an interesting similarity is evident between the intensity-dependent increasing of the dissipation times that correlate with the flattening of the exponential decay and the characteristic dispersity of the CC transport in random-solid systems. This dispersive CC-transport feature is clearly observable with P3HT, especially at the low electric field values, since the CC-transit times are significantly longer than those of any other case, and therefore, under that situation, sufficient time exists for the CCs to relax within a broad density of states. The shapes of the TPC traces in this study, however, are significantly nondispersive compared with those of the conventional TOF signals. This difference can be easily recognized when the signals are plotted on a graph with a loglog scale that is not shown in this study.

The CC mobility corrected with the RC time and the saturation effect shows that the intensity-dependent values of both PTB7 and P3HT converged to a faster common CC mobility with the decreasing of the incident photon density, while the CC mobilities of PTB7 at the high incident photon densities are significantly faster than those

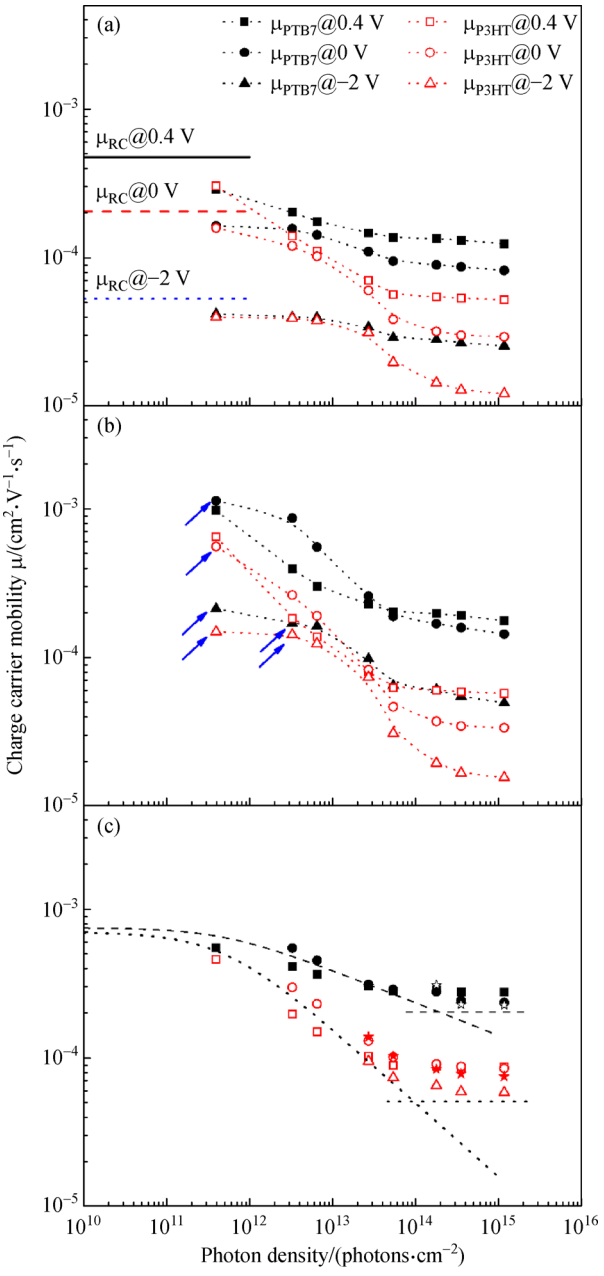

Fig. 8 Plots of the CC mobility vs. the incident photon density. (a) Native $\tau_{1/e}$ CC mobility; (b) CC mobility corrected by the RC-time-constant effect; (c) CC mobility corrected by the RC time constant and the saturation effect. The calculated CC mobilities for which an RC time of 0.45 μs was used at the external biases of 0.4 V (straight line), 0 V (dash line), and –2 V (dot line) are marked in (a). The points marked with arrows in (b) are for the assignment of the CC mobilities that were significantly affected by the RC time.

of P3HT; however, this does not mean that the spectrally resolved efficiency of PTB7 should be higher, because the EQE of P3HT is higher than that of PTB7 and the ExtQE of P3HT at $0.4V_{ext}$ is also higher than that of PTB7 at the same V_{ext} value. This finding means that even though the mobility values were estimated under a different condition alone, they cannot serve as a determinant factor for the

efficiency. And the mobilities that are shown here should include terms that are related to the delayed CC extraction due to the space charge-limited current at the high incident photon densities; consequently, an extension of the dissipation time should occur, thereby resulting in a longer transit time, as shown in Fig. 8. However, the CC loss mainly occurs at the beginning of the TPC process due to the CC interaction does not seem to significantly affect the shortening of the transit time. This could be shown by the overlapped TPC traces at the high incident photon densities; meanwhile, the decreasing CC amount increased with the increasing of the incident photon density.

Figure 9 shows schematic representations of two-dimensional energy level maps of a disordered system (a) for a high electric field and (b) for a low electric field in terms of the hopping formalism [32]. Detailed description about the map is shown in the ESM part as "Description for Fig. 9 in the manuscript". The gray-coloured pixels are the sites that can be easily used by the CCs during their transportation, while the black-coloured pixels are deep traps, and the white-coloured pixels are sites of a relatively high energy that can be disturbing factors for the CC transportation. On those schematic maps, the bold dash lines with the balls and arrows express the possible transportation that can occur through the gray-coloured pixels. It is easy to recognize the difficulty regarding the identification of proper neighbouring hopping sites at the low electric field. However, the CC movement should be affected by not only the site energies, but also by the trapped as well as even the simply populated CCs, in addition to the various excited species, as soon as the whole picture is considered. Therefore, many-body ensemble matter is more realistic, especially for the ss-device operating condition, where they are also more practical. Furthermore, this kind of picture enables the assumption that the CC photogeneration must be considered with various factors of CC-transport phenomena if a generation is not the event of a single isolated excited moiety.

Consistent with the intention of the demonstrative maps, a higher number of CC-transport pathways were found at the higher electric fields compared with the lower electric

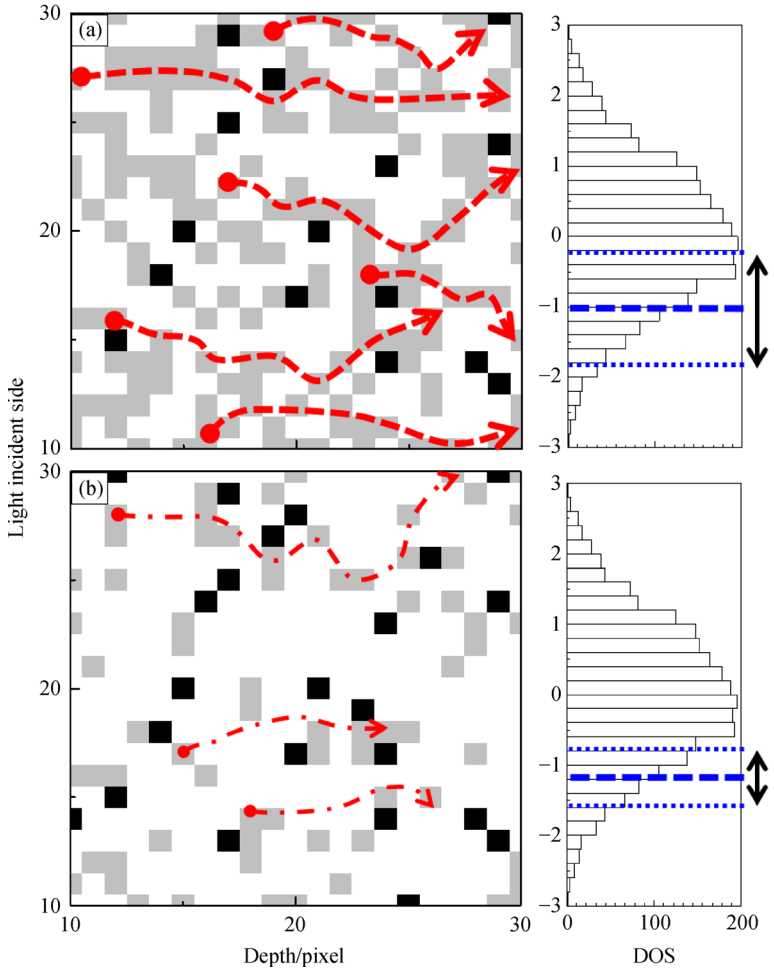

Fig. 9 Two-dimensional energy-level maps of the active layers with the corresponding density of states: (a) for a high electric field and (b) for a low electric field.

fields, especially on a governed molecular localization, and this explains the dominant incoherent nature of the disordered potential-energy landscapes that are based on loosely packed amorphous-solid systems. This aspect can be compared with the maximum CC concentration in an active layer for an operational moment, which can be also interpreted as the maximum activated channels of a system. Obviously, a CC mobility that is experimentally estimated using the TPC nearby the space charge-limited current regime possesses CC-interaction terms, while the conventional TOF and the single-electron kinetic Monte Carlo simulation mainly possess disorder-effect-controlled CC drift-velocity terms. Therefore, those unperturbed mobility results should be carefully scaled for their application in the attainment of an understanding of the ss operations of some features that are closely connected to the space charge-limited current character; this is meaningful for the ss operations of solar cell devices including diverse applications like light-emitting diode lighting and lasing, where a high current is used.

When the number of pathways can be predicted at a given V_{total}, it is feasible to gain an understanding of the incident photon density-dependent TPC behaviours, especially when the CCs were generated not only at the front side of the active layer. The salient matter here is whether the numbers of the generated CCs are over the space charge-limited current limit or not. At the conditions beyond the space charge-limited current limit (i.e., bulk limited-CC-transport possibility at a certain drift velocity), it is necessary for some of the CCs to experience longer delay times before the next hopping chance appears, as shown in Fig. 9. Consequently, it might be necessary to consider a higher dissipation probability, and this can be explained by means of, for example, the bimolecular electron-hole recombination. The TPC results that show a part of the complex ensemble behaviours of the CC extraction should also affect the CC photogeneration, because the CC generation should be strongly limited by the initial separation, which needs to be connected to a sufficient spatial possibility to enable the escape for a given system.

In addition to the bulk limit, various interfacial limits can play important roles, even without an energetic barrier. This is precisely the point where the chemical structure of the involved molecules and their arrangement in a solid, often discussed as the morphology, should be connected to the ensemble-CC dynamics, especially when the CC-related population exceeds the space charge-limited current range. Therefore, the mobility cannot only be a function of the electric field and the temperature, as it is also a function of the excitation intensity, the CC concentration, the morphology, and the device structure, among others. Further, these parameters are crucial for the attainment of an understanding of the insights regarding a working device under the usual operating condition, where the ensemble-CC behaviors are more important.

4 Conclusions

TPC measurements were performed under various external-bias voltages for a wide range of incident photon densities with conventionally optimized BHJ devices comprising 80 nm thick active layers consisting of the P3HT and PTB7 electron-donating polymers, which had been blended with proper electron-accepting fullerene derivatives.

It became evident that the TPC traces were saturated at the high incident photon densities, where the photocurrent density exceeds the space charge-limited current level of its corresponding dark J–V characteristics. After the correction of the saturated TPC traces, the numbers of the photogenerated CCs from the maximum photocurrent densities and the total numbers of the extracted CCs from the integrated TPC traces were simultaneously estimated. These values were then used to calculate the EQEs and ExtQEs of the CC collection during a laser-pulse-induced TPC process. The EQEs are electric field- and incident photon density-dependent, while the ExtQEs are significantly independent of the incident photon density. The P3HT system, however, showed a pronounced electric field dependence, whereas PTB7 showed a weak electric field dependence. The average EQE and IQE amplitudes under TPC condition at the low incident photon densities are ~10% and ~13%, respectively; these values are significantly smaller than those obtained with the ss characterization. Nevertheless, those values seem reasonable when the short and intense laser-pulse excitation is taken into account.

After the spanning of the basic quantitative framework for the whole CC dynamics, the decay shapes of the TPC traces were analysed to further investigate the CC-extraction dynamics. However, the dissipation shapes can be affected by inadvertent influences due to the CC losses that occur during the extraction (e.g., immobilization by trapping and/or annihilation by bimolecular recombination). It also became evident that the decay shapes of the TPC traces were significantly affected by the RC time constant, especially at the higher electric fields where the CCs move very quickly.

Therefore, the statistical corrections for the RC time and the saturation effect were performed for the whole sets of the TPC results. After that, mobility values that are dependent on the incident photon density, hence the approximate CC concentration, but that are electric field-independent, were obtained regardless of the material system. With the decreasing of the incident photon density, the CC mobilities of both systems increased and converged to the virtually same value of $\sim 7 \times 10^{-3}$ $cm^2 \cdot V^{-1} \cdot s^{-1}$; however, the mobility slopes as functions of the incident photon density are distinctively deviate between the two material systems. The CC mobilities of PTB7 seem significantly faster than those of P3HT, even at the higher

incident photon density range; this does not affect the CC-collection probability, as described by the EQE and the IQE in this study. Thus, it seems that the transit times, and hence the extracted mobilities, of this study are not strongly affected by any other loss mechanism, since the most number of CC losses seemed to occur mainly during the excitation-pulse incident.

It could also be shown that the mobility values that were obtained with the devices with thin active layers can be used to study various material systems. The use of an active layer that is thinner than that of the conventional TOF method is surely beneficial to maintain a consistency with the optimized device structure; if the RC effect is too strong, it can be removed using the moderate electric field strengths. Furthermore, a statistical analysis for which TPC experimental results are used can provide various material-specific parameters that depict the CC dynamics therein.

Acknowledgements This study was supported by the projects of National Research Foundation of Korea (Project No.: NRF-2018R1D1A1B07048843, Ministry of Education and NRF-2018K2A9A2A06023902, Ministry of Science and ICT) in addition to the program for Changbaishan Scholars of Jilin Province, China.

Electronic Supplementary Material Supplementary material is available in the online version of this article at https://doi.org/10.1007/s11705-020-1976-z and is accessible for authorized users.

References

1. Krebs F C, Espinosa N, Hösel M, Søndergaard R R, Jørgensen M. Rise to power—OPV-based solar parks. Advanced Materials, 2014, 26(1): 29–39
2. Jiang K, Wei Q, Lai J Y L, Peng Z, Kim H K, Yuan J, Ye L, Ade H, Zou Y, Yan H. Alkyl Chain tuning of small molecule acceptors for efficient organic solar cells. Joule, 2019, 3(19): 3020–3033
3. Lin Y, Adilbekova B, Firdaus Y, Yengel E, Faber H, Sajjad M, Zheng X, Yarali E, Seitkhan A, Bakr O M, El-Labban A, Schwingenschlögl U, Tung V, McCulloch I, Laquai F, Anthopoulos T D. 17% efficient organic solar cells based on liquid exfoliated WS_2 as a replacement for PEDOT:PSS. Advanced Materials, 2019, 31(46): 1902965–1902965
4. Yang W S, Park B W, Jung E H, Jeon N J, Kim Y C, Lee D U, Shin S S, Seo J, Kim E K, Noh J H, Seok S I. Iodide management in formamidinium-lead-halide–based perovskite layers for efficient solar cells. Science, 2017, 356(6345): 1376–1379
5. Green M A. The path to 25% silicon solar cell efficiency: history of silicon cell evolution. Progress in Photovoltaics: Research and Applications, 2009, 17(3): 183–189
6. Torto L, Cester A, Rizzo A, Wrachien N, Gevorgyan S A, Corazza M, Krebs F C. Model of organic solar cell photocurrent including the effect of charge accumulation at interfaces and non-uniform carrier generation. Journal of Electron Devices Society, 2016, 4(6): 387–395
7. Menke S M, Ran N A, Bazan G C, Friend R H. Understanding energy loss in organic solar cells: toward a new efficiency regime. Joule, 2018, 2(1): 25–35
8. Park H, An J, Song J, Lee M, Ahn H, Jahnel M, Im C. Thickness-dependent internal quantum efficiency of narrow band-gap polymer-based solar cells. Solar Energy Materials and Solar Cells, 2015, 143: 242–249
9. Moulé J, Bonekamp J B, Meerholz K. The effect of active layer thickness and composition on the performance of bulk-heterojunction solar cells. Journal of Applied Physics, 2006, 100(9): 094503-1, 094503–094507
10. Song J, Lee Y, Jin B, An J, Park H, Park H, Lee M, Im C. Connecting charge transfer kinetics to device parameters of a narrow band-gap polymer-based solar cell. Physical Chemistry Chemical Physics, 2016, 18(38): 26550–26561
11. Cappel U B, Feldt S M, Schöneboom J, Hagfeldt A, Boschloo G. The influence of local electric fields on photo-induced absorption in dye sensitized solar cells. Journal of the American Chemical Society, 2010, 132(26): 9096–9101
12. Pivrikas A, Sariciftci N S, Juska G, Österbacka R. A review of charge transport and recombination in polymer/fullerene organic solar cells. Progress in Photovoltaics: Research and Applications, 2007, 15(8): 677–696
13. Gao Y, Pivrikas A, Xu B, Liu Y, Xu W, van Loosdrecht P H M, Tian W. Measuring electron and hole mobilities: charge selective CELIV. Synthetic Metals, 2015, 203: 187–191
14. Park H, Jin B, Kim Y, Im C, An J, Park H, Tian W. Intensity-dependent transient photocurrent of organic bulk heterojunction solar cells. Journal of the Korean Physical Society, 2017, 70(2): 177–183
15. Im C, Bässler H, Rost H, Hörhold H H. Hole transport in polyphenylenevinylene-ether under bulk photoexcitation and sensitized injection. Journal of Chemical Physics, 2000, 113(9): 3802–3807
16. Bässler H, Köhler A. Unimolecular and supramolecular electronics: charge transport in organic semiconductors. Topics in Current Chemistry, 2012, 312: 1–65
17. Howard I A, Hodgkiss J M, Zhang X, Kirov K R, Bronstein H A, Williams C K, Friend R H, Westenhoff S, Greenham N C. Charge recombination and exciton annihilation reactions in conjugated polymer blends. Journal of the American Chemical Society, 2010, 132(1): 328–335
18. Di Nuzzo D, van Reenen S, Janssen R A J, Kemerink M, Meskers S C J. Evidence for space charge-limited conduction in organic photovoltaic cells at open-circuit conditions. Physical Review. B, 2013, 87(8): 085207-1, 085207–085211
19. Cowan S R, Banerji N, Leong W L, Heeger A J. Charge formation, recombination, and sweep-out dynamics in organic solar cells. Advanced Functional Materials, 2012, 22(6): 1116–1128
20. Hwang I, Greenham N C. Modeling photocurrent transients in organic solar cells. Nanotechnology, 2008, 19(42): 424012
21. Credgington D, Durrant J R. Insights from transient optoelectronic analyses on the open-circuit voltage of organic solar cells. Journal of Physical Chemistry Letters, 2012, 3(11): 1465–1478
22. Sudheendra Rao K, Mohapatra Y N. Open-circuit voltage decay transients and recombination in bulk-heterojunction solar cells. Applied Physics Letters, 2014, 104(20): 203303
23. Miyake M, Nakajima H, Hemmi A, Yahiro M, Adachi C, Soh N,

Ishimatsu R, Nakano K, Uchiyama K, Imato T. Performance of an organic photodiode as an optical detector and its application to fluorometric flow-immunoassay for IgA. Talanta, 2012, 96: 132–139

24. Jahnel M, Thomschke M, Fehse K, Vogel U, An J D, Park H, Leo K, Im C. Integration of near IR and visible organic photodiodes on a complementary metaloxidesemi-conductor compatible backplane. Thin Solid Films, 2015, 592(Part A): 94–98
25. Jŭska G, Genevĭcius K, Nekrăsas N, Sliaŭzys G. Charge carrier transport, recombination, and trapping in organic solar cells studied by double injection technique. IEEE Journal of Selected Topics in Quantum Electronics, 2010, 16(6): 1764–1769
26. McNeill C R, Hwang I, Greenham N C. Polaronic interaction of photocurrent transients in all-polymer solar cells: trapping and detrapping effects. Journal of Applied Physics, 2006, 106: 024507-1–024507-8
27. Hahn T, Tscheuschner S, Kahle F J, Reichenberger M, Athanasopoulos S, Saller C, Bazan G C, Nguyen T Q, Strohriegl P, Bässler H, Köhler A. Monomolecular and bimolecular recombination of electronhole pairs at the interface of a bilayer organic solar cell. Advanced Functional Materials, 2017, 27(1): 1604906
28. Valouch S, Nintz M, Kettlitz S W, Christ N S, Lemmer U. Thickness-dependent transient photocurrent response of organic photodiodes. IEEE Photonics Technology Letters, 2012, 24(7): 596–598
29. Kniepert K, Neher D. Effect of the RC time on photocurrent transients and determination of charge carrier mobilities. Journal of Applied Physics, 2017, 122(19): 195501
30. Kettlitz S W, Mescher J, Christ N S, Nintz M, Valouch S, Colsmann A, Lemmer U. Eliminating RC-effects in transient photocurrent measurements on organic photodiodes. IEEE Photonics Technology Letters, 2013, 25(7): 682–685
31. Zhang D, Allagui A, Elwakil A S, Nassef A M, Rezk H, Cheng J, Choy W C H. On the modeling of dispersive transient photocurrent response of organic solar cells. Organic Electronics, 2019, 70: 42–47
32. Bässler H. Charge transport in disordered organic photoconductors a Monte Carlo simulation study. Physica Status Solidi. B, Basic Research, 1993, 175(1): 15–56
33. Gupta S K, Sharma A, Banerjee S, Gahlot R, Aggarwal N, Deepak, Garg A. Understanding the role of thickness and morphology of the constituent layers on the performance of inverted organic solar cells. Solar Energy Materials and Solar Cells, 2013, 116: 135–143
34. Liu F, Zhao W, Tumbleston J R, Wang C, Gu Y, Wang D, Briseno A L, Ade H, Russell T P. Understanding the morphology of PTB7·PCBM blends in organic photovoltaics. Advanced Energy Materials, 2014, 4(5): 1301377
35. Longeaud C, Main C. Deconvolution of the transient photocurrent signals: application to the study of the density of states of a BTO crystal. Journal of Physics Condensed Matter, 2008, 20(13): 135217